

Direct Iterative Reconstruction of Computed Tomography Trajectories: Reconstruction from limited number of projections with DIRECTT

Sotirios Magkos,^{1, a)} Andreas Kupsch,¹ and Giovanni Bruno^{1, 2}

¹⁾*Bundesanstalt für Materialforschung und -prüfung (BAM), Unter den Eichen 87, 12205 Berlin, Germany*

²⁾*University of Potsdam, Institute of Physics and Astronomy, Karl-Liebknecht-Str. 24-25, 14476 Potsdam, Germany*

X-ray computed tomography has many applications in materials science and non-destructive testing. While the standard filtered back-projection reconstruction of the radiographic data sets is fast and simple, it typically fails in returning accurate results from missing or inconsistent projections. Among the alternative techniques that have been proposed to handle such data is the Direct Iterative REconstruction of Computed Tomography Trajectories (DIRECTT) algorithm. We describe a new approach to the algorithm, which significantly decreases the computational time, while achieving a better reconstruction quality than that of other established algorithms.

I. INTRODUCTION

Since the 1980s, X-ray computed tomography (XCT) has found many applications in materials science and non-destructive testing^{1–6}. The basic principle of XCT is that an X-ray beam is attenuated, because of absorption or scattering, while it propagates through a sample. The part of the beam that traverses the sample is typically recorded in the form of (radiographic) 2D images by a detector. Such images are recorded for different angular positions of the rotating sample. Through mathematical reconstruction⁷ of these images, the 3D-resolved attenuation coefficient μ of different parts of the sample can be determined.

The standard reconstruction strategy is the *filtered back-projection* (FBP). Back-projection refers to the smearing of the projected values (recorded in each detector pixel) back in the direction of the X-ray source. This procedure does not return the exact attenuation values, since the value of each element of the reconstructed image is computed through integration over the complete path of the corresponding rays. Filtering the projections with a high-pass filter⁸ results in a sampling pattern that is more appropriate to the circular projection acquisition strategy, and a more accurate reconstruction. The algorithm proposed by Feldkamp, Davis, and Kress (FDK)⁹ is the standard FBP algorithm used for the reconstruction of cone beam data acquired over a circular scan.

While FBP is very fast, it typically fails in producing an accurate reconstruction from missing or inconsistent projections. Moreover, it weights all rays equally, meaning that certain effects, such as beam-hardening, can give rise to severe artefacts in the reconstruction. In the above cases, iterative reconstruction techniques can serve as alternatives to FBP. With iterative techniques, the reconstructed image is calculated as the solution of a system of linear equations. Numerous approaches are used for the solution of such systems, be it either algebraic¹⁰ or statistical¹¹.

This article provides an overview of recent advances on the *Direct Iterative REconstruction of Computed Tomography Trajectories* (DIRECTT) algorithm. While previously re-

ported results^{12–14} clearly demonstrated how DIRECTT was able to produce more accurate reconstructions compared to conventional techniques, the time required for each iteration was impractically high. Here we describe how a new approach can significantly shorten the computational time, while maintaining the improved reconstruction quality that was demonstrated previously in the works of Lange et al.^{12–14}.

II. MATERIALS AND EXPERIMENTAL METHODS

A. Sample images

Two data sets were used to test the performance of the DIRECTT algorithm:

1. A set of 3000 projections of a metal matrix composite (MMC) plate were acquired over 180° with a parallel beam at the BAMline¹⁵ of the BESSY synchrotron radiation facility in Berlin, Germany. The MMC was an AlSi₁₂CuMgNi alloy reinforced with 7 vol% of Al₂O₃ short fibers and 15 vol% SiC particles (see also Ref. 16). The whole composite was produced by squeeze casting. The diameter of the cylindrical sample was 1 mm. A pco.4000 CCD camera of 4008×2672 pixels was used for the measurement. The nominal pixel size was 9 μm and a 20× magnification resulted to a linear voxel size of 0.44 μm . Monochromatic radiation of 25 keV was selected and the acquisition time per projection was 3 s¹⁷. The incident cross section was narrowed by a slit system to the detector field-of-view (FoV) in order to reduce detector backlighting¹⁸.
2. A set of 3000 cone-beam projections of a concrete rod with a diameter of 30 mm was acquired over 360° on an in-house GE vltomelx L 300 scanner. The scanner was equipped with a 2024×2024 PerkinElmer detector with a pixel size of 0.2 mm. The acquisition time per projection was 6 s, and the source-object and source-detector distances were set to 81.44 mm and 1018 mm, respectively, for a voxel size of 0.016 mm (magnification of 12.5). The voltage and current settings of the

^{a)}Electronic mail: sotirios.magkos@bam.de

source were set to 140 kV and 80 μ A, and a 0.5 mm Cu prefilter was used.

B. Software

In the scope of this article, the DIRECTT algorithm was applied on the two data sets using the Python programming language. The forward- and back-projection operations were performed via the open-source ASTRA toolbox¹⁹. The use of ASTRA allows computationally demanding operations to be offloaded to a graphics processing unit (GPU) using the CUDA language. In addition, several algorithms, including the FBP, the Simultaneous Iterative Reconstruction Technique (SIRT)²⁰ and a Conjugate Gradient (CG)²¹ method based on the Krylov subspace, are available in the toolbox for reconstruction without any intervention by the user¹⁹.

III. BASIC PRINCIPLES OF THE DIRECTT ALGORITHM

DIRECTT as proposed by Lange *et al.*¹² operates by selectively back-projecting filtered projections in an iterative process, where the focus is on the precise projection. Rather than directly solving the inverse problem, the aim of the algorithm is to find the best solution (reconstruction) possible by numerically mimicking the actual physical projection process (e.g. finite focal spot size²², strong absorbers²³). Unlike most iterative techniques, the starting point of DIRECTT is an empty reconstruction array. During the first iteration, the algorithm determines which trajectories (among all the traceable trajectories across the projections) are the most dominant. Only the elements of the reconstruction array that correspond to these trajectories are updated after the projections have been filtered. At the end of the iteration, the Radon transform of the reconstruction array is computed and subsequently compared to the *measured* projections. The described process is repeated for the calculated *difference*. The algorithm is terminated when the variance of these residual projections is sufficiently close to zero.

The technique has been shown capable of returning reconstructed images that are of superior quality to the ones computed by standard FBP and even by some other iterative algorithms^{13,24,25}. However, its application through the calculation of all the trajectories was computationally expensive for large data sets, mainly because of the convolution operation, which is required for the filtering of the residual projections during each iteration. An additional drawback of repeatedly filtering the projections is the increasing presence of salt-and-pepper noise in the reconstructed images. We solved this problem with an alternative approach described below. We will in fact demonstrate how to determine which elements of the reconstruction array should be updated during each iteration without the use of any filtering prior to the back-projection.

During back-projection, the greyscale value of each element of the reconstructed image is computed through integration over the complete path of the corresponding rays.

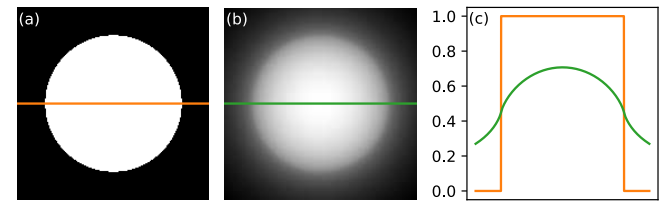


FIG. 1. (a) Model of a homogeneous disc; (b) Reconstruction of the disc by back-projection; (c) Profiles through the centre of the model (orange) and its reconstruction (green).

Therefore, the voxels around the centre of mass of the sample have disproportionately higher values compared to the voxels closer to the edges of the sample. An example is shown in Fig. 1: the back-projected image of a homogeneous disc resembles a disc with a blurred edge to its background, and with density decreasing as a function of distance from its centre of mass. Based on the above observation, it is safe to assume that any elements of the back-projected image with a greyscale value greater or equal to B_c , the value of the element that corresponds to the centre of mass of the sample, would correspond to the most dominant trajectories within the projections. Regardless of the example used, the shape of the sample does not introduce any limitations to the performance of the algorithm.

During the first iteration of this version of DIRECTT, only the elements of the back-projected image with a value greater or equal to B_c are selected. This selection is rescaled, so that its largest grey value remains unaltered and its lowest decreases to zero. From this point onward, the performed operations match their equivalents from the original version of the algorithm: the selection is added to the initially empty reconstruction array; the now partially reconstructed image is then projected according to the projection geometry of the measurement; the resulting projections are subtracted from the measured ones. All these steps are demonstrated in the top row of Fig. 2.

During each subsequent iteration, a new value B'_c is used for the selection of the elements that will be updated. B'_c is proportional to the actual weight of the residual projections:

$$B'_c = \frac{\text{Weight of residual projection}}{\text{Weight of measured projections}} \times B_c. \quad (1)$$

Each selection is added to the reconstruction array, which is projected in its current form, so that new and further reduced residual projections can be calculated. The criterion for the termination of the algorithm is whether the weight of the computed Radon transform is equal to that of the measured projections, not the variance of the residual projections as was the case for the original version of DIRECTT.

The middle rows of Fig. 2 demonstrate all steps of the second and seventh iteration. While the reconstruction array is building up, its Radon transform resembles more and more the measured projection. Accordingly, the residual projections tend to zero and the back-projected image contains increasingly less information. During the final iteration (bottom row of Fig. 2), the computed Radon transform has the same weight

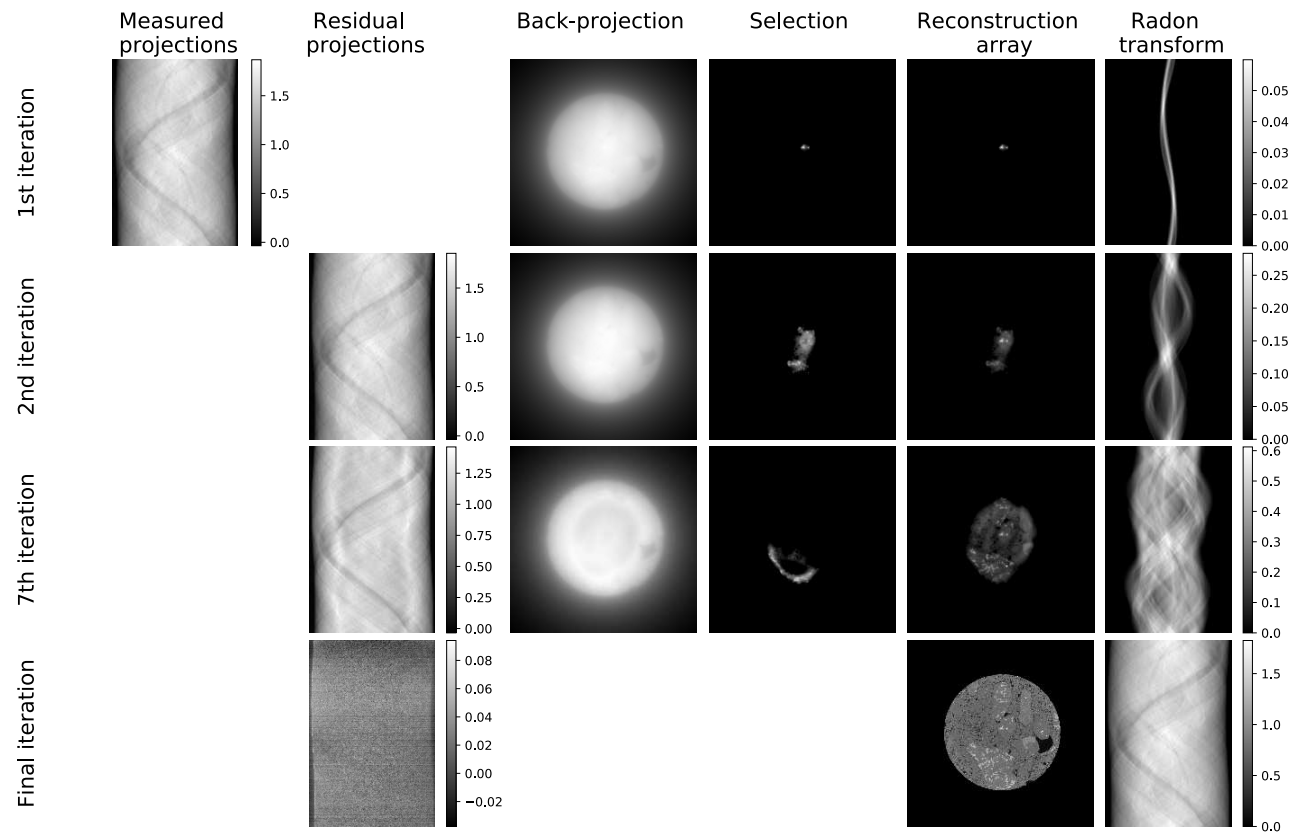


FIG. 2. The different steps of the DIRECTT algorithm for the first, second, seventh and final iteration of reconstruction of the concrete sample. The greyscale values that are described by the bars correspond to the attenuation integral values.

TABLE I. Average time required for the execution of a single iteration of each algorithm for a 2024×2024 slice.

Algorithm	Average time per iteration (s)
FBP	2.71 ± 0.03
SIRT	0.87 ± 0.05
CG	0.88 ± 0.01
DIRECTT	1.38 ± 0.01
DIRECTT (Lange <i>et al.</i> ^{12–14})	3.62 ± 0.02

as the measured projections and the residual projections consist mainly of noise; therefore, the algorithm is terminated.

IV. RESULTS

Four different algorithms were used for the reconstruction of the two data sets. Three of them are available from the ASTRA toolbox: FBP, SIRT and CG. SIRT and CG were programmed to perform a fixed number of 70 and 500 iterations, respectively. The number of iterations for each algorithm was determined to be the number that produces images with a good balance between noise and blur. The quantification of this balance is attempted in the Discussion section.

The other algorithm used was DIRECTT. No fixed number of iterations was programmed for it. As we mentioned in section III, DIRECTT is terminated when the residual projections have the same weight as the measured projections. Table I lists the average time required for the execution of a single iteration of each algorithm (including the original version of DIRECTT) for one slice through the concrete volume on a computer equipped with an NVIDIA GeForce GTX 1080 Ti GPU. In the case of FBP, the time listed refers to the total time required and was calculated as the mean value after repeating the operation 50 times.

A. Simulation of the missing wedge problem

A slice through the volume of the MMC sample as reconstructed by each of the algorithms is shown in Fig 3. SIRT and DIRECTT have returned images that are less noisy than the ones by FBP and CG.

In order to evaluate the performance of the algorithms in the case when the sample cannot be rotated over the full 180° , the last 1000 projections were removed from the data set, thus creating a missing wedge of 60° . The reconstruction of the slice from this limited set of projections is shown in Fig. 4. Again, the images returned by SIRT and DIRECTT appear to be an

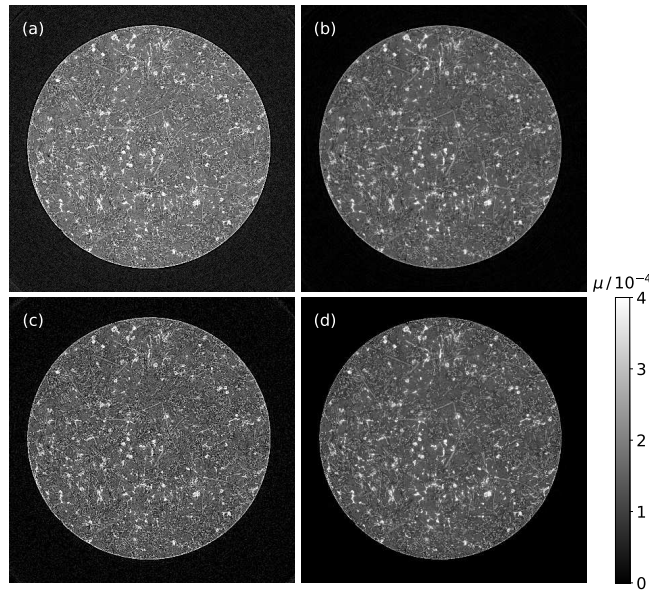


FIG. 3. Slice through the MMC sample volume as reconstructed from 3000 projections by (a) FBP, (b) SIRT (500 iterations), (c) CG (70 iterations), and (d) DIRECTT (126 iterations). The μ scales described by the bars on the right were set equally for all subfigures.

improvement compared to FBP and CG, in terms of noise. In addition, while the shape of the sample in the other three images appears distorted as a result of the missing wedge, this distortion is less apparent in the case of DIRECTT. This is another indication of the ability of DIRECTT to accurately estimate how the different densities, which result to the measured projections, are distributed in the space.

B. Simulation of sparse-sampling acquisitions

A slice through the volume of the concrete as reconstructed by each of the four reconstruction algorithms is shown in Fig. 5. The images reconstructed by the iterative algorithms are comparable to the one by FBP, but multiple iterations of each algorithm were required.

In order to evaluate the performance of the algorithms in a case when fewer projections are acquired over a full rotation of the sample, certain projections were evenly and progressively removed from the data set and new reconstructions were computed from 1500, 1000, 750, 600 and 500 projections. The reconstruction of the slice from 500 projections is shown in Fig. 6. There is an obvious decrease in the quality of the reconstructed image returned by FBP compared to the full number of projections. The quality of the reconstructions returned by the iterative algorithms has also decreased, but to a lesser extent.

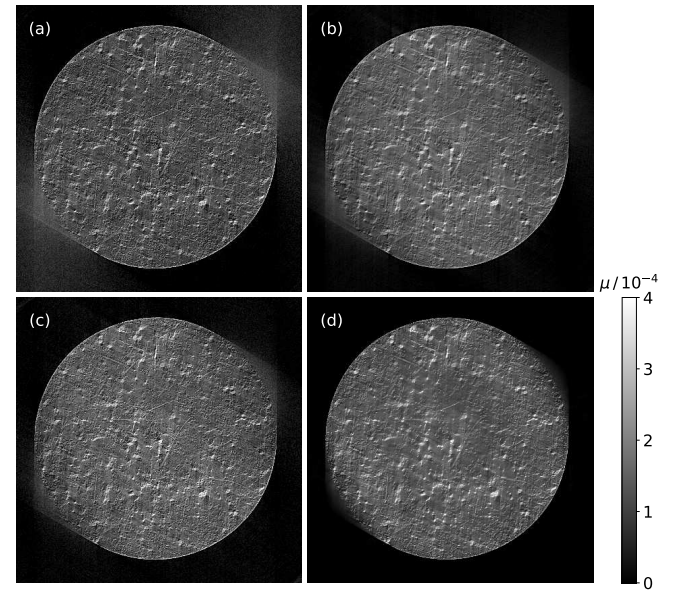


FIG. 4. Slice through the MMC sample volume as reconstructed from 2000 projections by (a) FBP, (b) SIRT (500 iterations), (c) CG (70 iterations), and (d) DIRECTT (112 iterations). The last 1000 projections were removed from the original data set, so to simulate an acquisition with a missing wedge of 60° . The μ scales described by the bars on the right were set equally for all subfigures.

TABLE II. Histogram entropy for the reconstructed images of the MMC sample.

Angular range	Histogram entropy			
	FBP	SIRT	CG	DIRECTT
180°	4.0	4.1	3.9	2.9
120°	4.2	4.4	4.1	3.2

V. DISCUSSION

A. Missing wedge reconstruction – MMC sample

A first evaluation of the quality of the reconstructed images is attempted using the histogram entropy metric²⁶. The histogram entropy is defined as

$$H = - \int p(\mu) \log[p(\mu)] d\mu, \quad (2)$$

where $p(\mu)$ is the distribution function of the grey values. The presence of homogeneously distributed noise maximizes the entropy, while the presence of sharp edges minimizes it²⁷. Since both noise and blur cause the entropy to increase, a low value of the metric should indicate a good balance between the two. The histogram entropy values for all images in Figs 3 and 4 are listed in Table II. The DIRECTT-reconstructed images have the lowest entropy for both angular ranges of projection.

Because the 3000 projections acquired during the measurement using a 4008×2672 CCD camera are significantly fewer than the optimal number according to the Nyquist

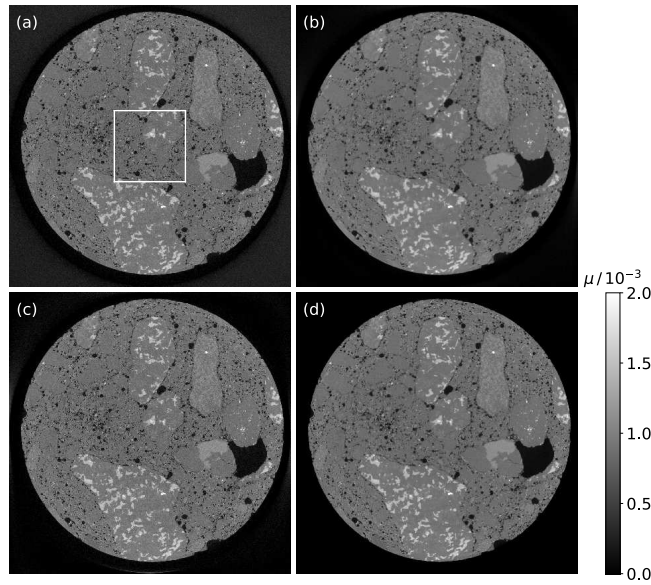


FIG. 5. Slice through the concrete sample volume as reconstructed from 3000 projections by (a) FBP, (b) SIRT (500 iterations), (c) CG (70 iterations), and (d) DIRECTT (151 iterations). The framed region in a) was used as a reference for the calculation of the quality metric values (see Discussion section). The μ scales described by the bars on the right were set equally for all subfigures.

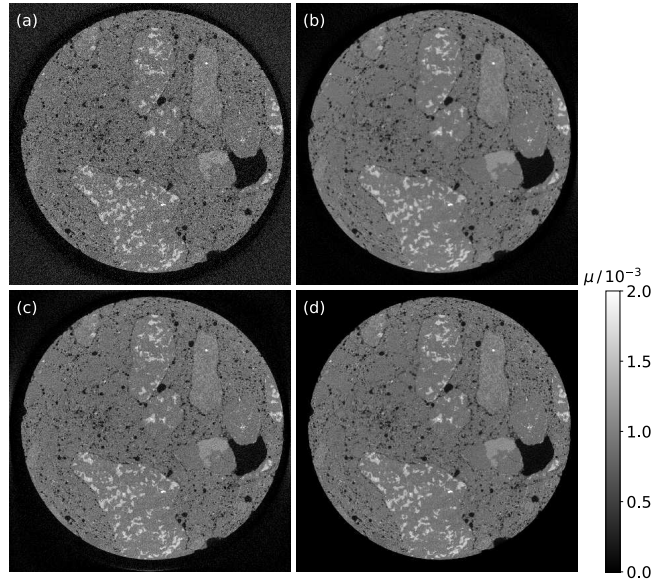


FIG. 6. Slice through the concrete sample volume as reconstructed from 500 projections by (a) FBP, (b) SIRT (500 iterations), (c) CG (70 iterations), and (d) DIRECTT (147 iterations). The μ scales described by the bars on the right were set equally for all subfigures.

criterion, no reconstructed image, including the one reconstructed by FBP, can be adequately close to the ground truth. The evaluation of any image using a full-reference metric is therefore meaningless. Instead, to evaluate the quality of the images reconstructed with the simulated missing wedge of 60° , their Radon transform over the full range

of 180° was computed. A circular mask of approximately the same radius as the actual sample was applied on all reconstructed images, except for the one reconstructed by DIRECTT, in order to diminish the effect of the distortion caused by the missing wedge. The transforms of a slice through each reconstructed volume (Fig. 4) are shown in Fig. 7 along with the measured projections. It is evident that the lower part of the sinograms, corresponding to the range between 120° and 180° , differs significantly from the original ones. The projections are blurred, and it is very difficult, if not impossible, to trace the continuation of any of the trajectories that are discernible in the upper part of the sinograms. This is much less the case for the projections of the DIRECTT-reconstructed volume. Even though the simulated missing projections are more blurred than the original ones, this lower part of the sinogram appears to be a reasonable continuation of the upper part, and certain trajectories can be traced all the way through it.

The fidelity of the simulated projections to the original ones, and thus the quality of each reconstructed volume, can be assessed by calculating the *Pearson correlation coefficient* (PCC)²⁸ between the corresponding projections according to the relation

$$\text{PCC}_{M,R} = \frac{\sigma_{M,R}}{\sigma_M \sigma_R}, \quad (3)$$

where $\sigma_{M,R}$ is the covariance, and σ_M , σ_R the standard deviation of the measured projections and the computed Radon transform, respectively. The PCC can range from +1 to -1, where 1 signifies total linear correlation, 0 no linear correlation, and -1 total negative linear correlation. The PCCs between each projection of the slice through the reconstructed volume and its corresponding measured projection are plotted as a function of the projection angle in Fig. 8. Within the range from 0° to 120° , the coefficients for all four reconstruction algorithms are around the optimal value of 1. However, they abruptly decrease within the range that corresponds to the missing projections. This decrease is lower for the DIRECTT-reconstructed volume, even after the circular mask has been applied to the other three volumes, proving that DIRECTT performs better than the rest of the algorithms at compensating for the missing wedge.

B. Sparse-sampling data – concrete sample

The histogram entropy values for the concrete sample as reconstructed from 3000, 1500, 1000, 750, 600 and 500 projections are listed in Table III. As the number of projections decreases, the image noise increases and the edges become less sharp, causing the histogram entropy to increase. The DIRECTT-reconstructed images have the lowest entropy for any number of projections.

Because the 3000 projections acquired during the measurement using a 2024×2024 detector are very close to the optimal number according to the Nyquist criterion, the quality of each reconstructed volume can be assessed through the calculation of two full-reference metrics:

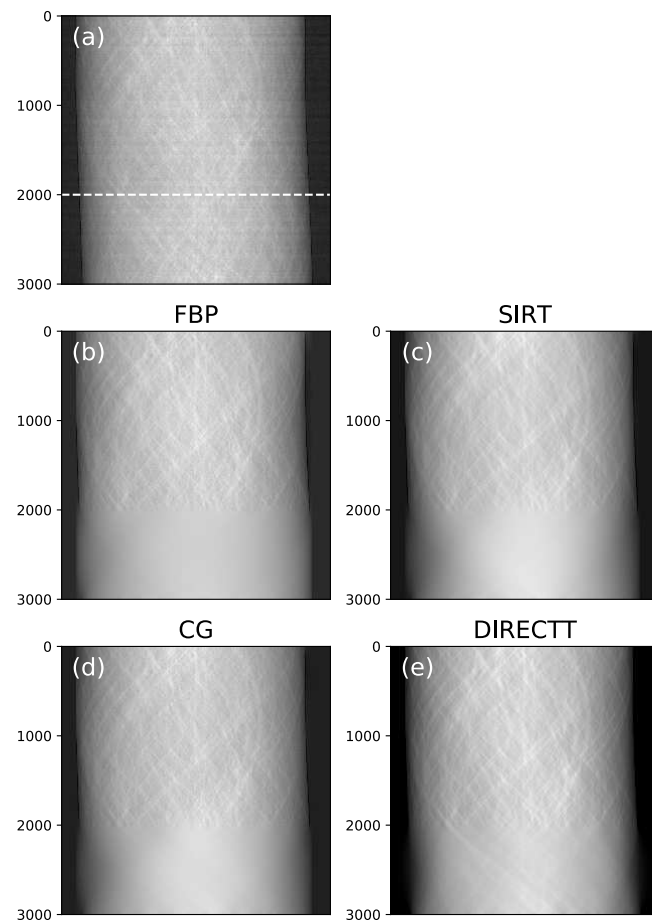


FIG. 7. (a) Measured projections of a slice through the MMC sample volume in the form of a sinogram. The projections below the dashed line were not used for the reconstruction of the images in Fig. 4, in order to simulate an acquisition with a missing wedge of 60° ; (b)-(e) Radon transforms of the reconstructed slices of Fig. 4 over the whole range of 180° . The lower part of each sinogram differs in varying degrees from the corresponding measured projections.

TABLE III. Histogram entropy for the reconstructed images of the concrete sample.

Number of projections	Histogram entropy			
	FBP	SIRT	CG	DIRECTT
3000	3.20	3.20	2.97	2.47
1500	3.33	3.26	3.12	2.51
1000	3.43	3.33	3.25	2.56
750	3.48	3.40	3.32	2.59
600	3.54	3.46	3.35	2.63
500	3.59	3.53	3.46	2.68

1. the *mean squared error* (MSE) calculates the average squared difference between the estimated values and the reference values²⁹;
2. the *universal quality index* (UQI) is calculated accord-

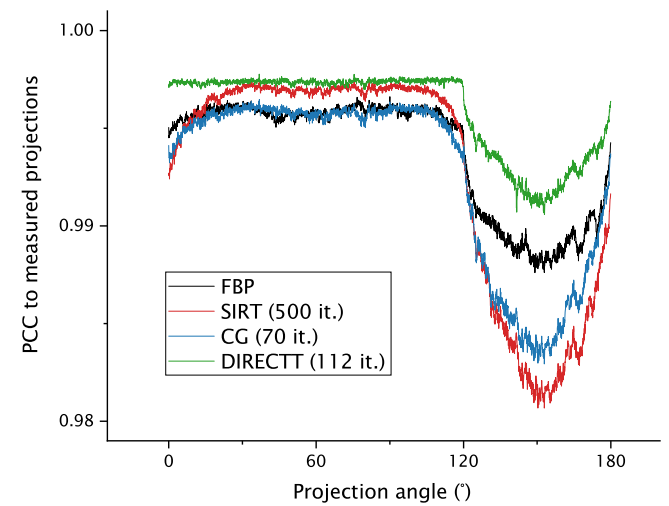


FIG. 8. The Pearson correlation coefficient between each projection of a slice through the reconstructed MMC sample volume and its corresponding measured projection.

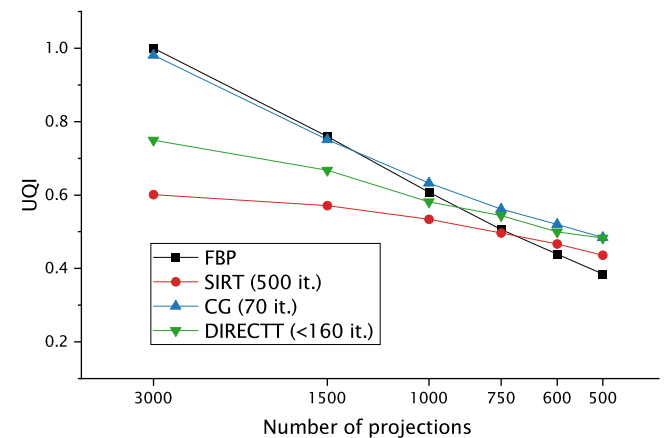
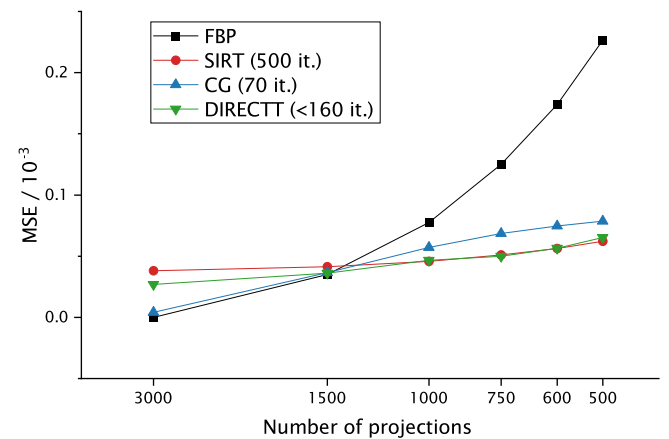


FIG. 9. Quality assessment of each reconstruction algorithm by the MSE and UQI metrics.

ing to the relation

$$UQI = \frac{2\mu_{\text{ref}}\mu_{\text{rec}}}{\mu_{\text{ref}}^2 + \mu_{\text{rec}}^2} \frac{2\sigma_{\text{ref,rec}}}{\sigma_{\text{ref}}^2 + \sigma_{\text{rec}}^2}, \quad (4)$$

where μ_{ref} and μ_{rec} are the mean values of the reference and the reconstructed image, respectively. The first factor of Eq. 4, which takes a value between 0 and 1, compares the luminance between the reference and the reconstructed image. The second factor has the same value range and measures how similar the contrasts of the images are^{30,31}.

Both metrics were calculated for a region of interest in the centre of the volume. The corresponding region of the FBP volume as reconstructed from the full 3000 projections (shown in Fig. 5a) was used as a reference. The calculated values for each metric and each reconstruction algorithm are plotted in Fig. 9 as functions of the number of projections which the volumes were reconstructed from.

According to the MSE, already for half the original number of projections, all four algorithms return an equally good result. After this point, the quality of the FBP reconstructions decreases much faster than the ones by the iterative algorithms. Both SIRT and DIRECTT appear to outperform CG slightly, but DIRECTT does so in a fraction of the iterations performed by SIRT.

According to the UQI, the quality of the FBP-reconstructed images decreases somewhat slower than estimated by the MSE. Their quality appears to be roughly linearly proportional to the logarithm of the number of projections. Still, the quality of the iterative reconstructions for 750 projections are at least as good as the ones by FBP. For a larger number of projections, CG appears to outperform DIRECTT, but the two algorithms return equally good results for fewer projections. However, DIRECTT needed to perform twice as many iterations as CG. In conclusion, DIRECTT returns the best reconstructed images from sparsely sampled data according to both the MSE and the UQI.

VI. SUMMARY

We have presented a new approach to the DIRECTT algorithm which has decreased the running time per iteration by more than half. We have successfully applied the algorithm on data sets of XCT projections in which two different types of limitations were introduced: a missing wedge of 60° (over the ideal 180°) in a case of a parallel-beam XCT, and a decreasing number of projections in a case of cone-beam XCT. Our results demonstrated that DIRECTT can outperform the standard FBP algorithm, as well as other established iterative algorithms.

ACKNOWLEDGMENTS

This work was part of the MUMMERING Innovative Training Network. The project has received funding from the

European Union's Horizon 2020 research and innovation programme under Marie Skłodowska-Curie grant agreement No. 765604. The authors kindly acknowledge Sergei Evsevlev and Dietmar Meinel (BAM) for providing the experimental data.

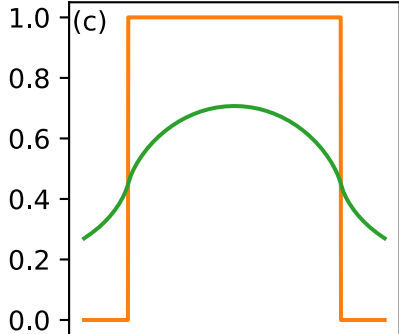
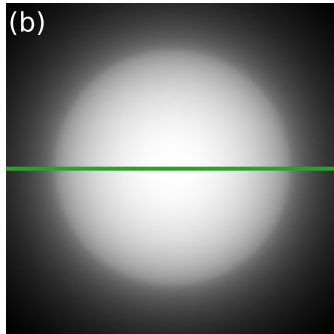
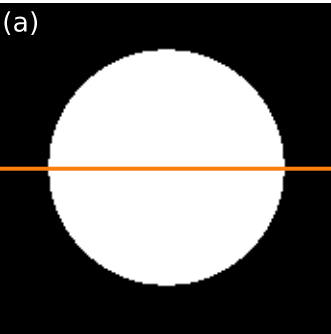
DATA AVAILABILITY STATEMENT

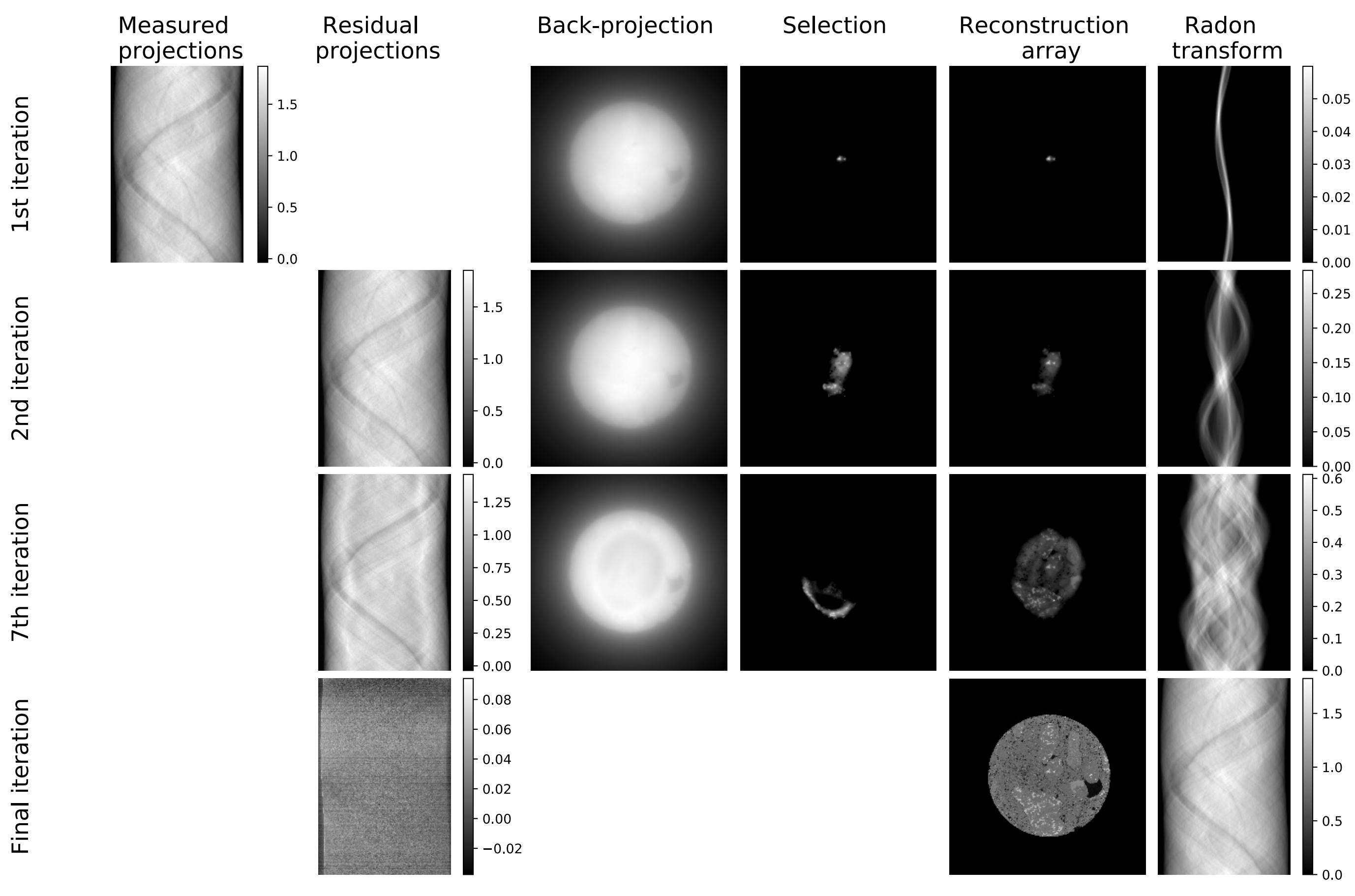
The data that support the findings of this study are available from BAM. Restrictions apply to the availability of these data, which were used under license for this study. Data are available from the authors upon reasonable request and with the permission of BAM.

REFERENCES

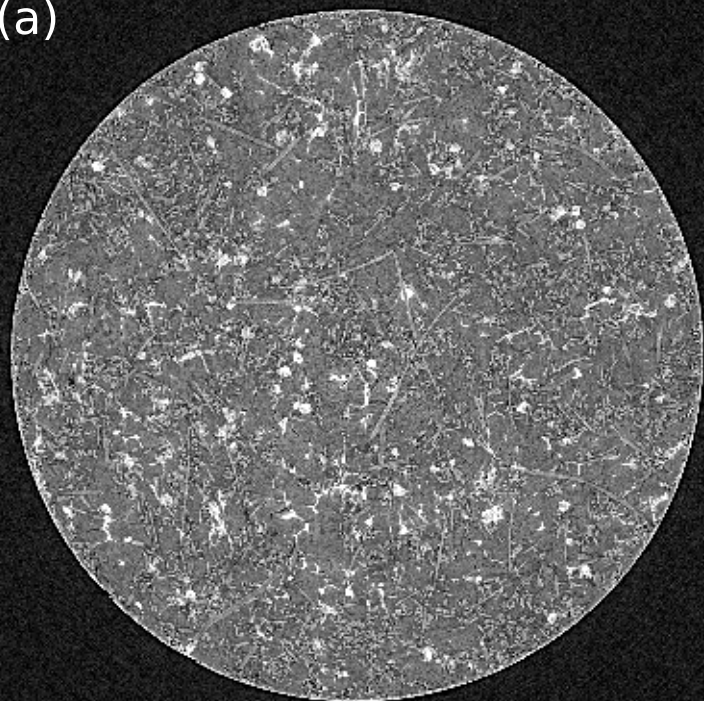
- ¹P. Reimers, J. Goebbels, H. P. Weise, and K. Wilding, "Some aspects of industrial non-destructive evaluation by X- and γ -ray computed tomography," *Nuclear Instruments and Methods in Physics Research* **221**, 201–206 (1984).
- ²W. B. Gilboy, "X- and γ -ray tomography in NDE applications," *Nuclear Instruments and Methods in Physics Research* **221**, 193–200 (1984).
- ³L. De Chiffre, S. Carmignato, J. P. Kruth, R. Schmitt, and A. Weckenmann, "Industrial applications of computed tomography," *CIRP Annals* **63**, 655–677 (2014).
- ⁴A. Kupsch, A. Lange, M. P. Hentschel, Y. Onel, T. Wolk, A. Staude, K. Ehrig, B. R. Miller, and G. Bruno, "Evaluating porosity in cordierite diesel particulate filter materials: Advanced X-Ray techniques and new statistical analysis methods," *Journal of Ceramic Science and Technology* **4**, 169–176 (2013).
- ⁵Y. Onel, A. Lange, A. Staude, K. Ehrig, A. Kupsch, M. P. Hentschel, T. Wolk, B. R. Miller, and G. Bruno, "Evaluating porosity in cordierite diesel particulate filter materials, Part 2: Statistical analysis of computed tomography data," *Journal of Ceramic Science and Technology* **05**, 13–22 (2014).
- ⁶D. Schob, I. Sagradov, R. Roszak, H. Sparr, R. Franke, M. Ziegenhorn, A. Kupsch, F. Lard, B. R. Miller, and G. Bruno, "Experimental determination and numerical simulation of material and damage behaviour of 3D printed polyamide 12 under cyclic loading," *Engineering Fracture Mechanics* **229**, 106841 (2020).
- ⁷A. C. Kak and M. Slaney, *Principles of Computerized Tomographic Imaging*, Classics in Applied Mathematics (Society for Industrial and Applied Mathematics, 2001) p. 335.
- ⁸L. A. Shepp and B. F. Logan, "Reconstructing interior head tissue from X-ray transmissions," *IEEE Transactions on Nuclear Science* **21**, 228–236 (1974).
- ⁹L. A. Feldkamp, L. C. Davis, and J. W. Kress, "Practical cone-beam algorithm," *Journal of the Optical Society of America A* **1**, 612–619 (1984).
- ¹⁰R. Gordon, R. Bender, and G. T. Herman, "Algebraic reconstruction techniques (ART) for three-dimensional electron microscopy and X-ray photography," *Journal of Theoretical Biology* **29**, 471–481 (1970).
- ¹¹K. Lange and R. Carson, "EM reconstruction algorithms for emission and transmission tomography," *Journal of Computer Assisted Tomography* **8**, 306–316 (1984).
- ¹²A. Lange, M. P. Hentschel, and A. Kupsch, "Computed tomography reconstructions by DIRECTT 2D model calculations compared to filtered backprojection," *Materials Testing* **50**, 272–277 (2008).
- ¹³A. Lange, A. Kupsch, M. P. Hentschel, I. Manke, N. Kardjilov, T. Arlt, and R. Grothausmann, "Reconstruction of limited computed tomography data of fuel cell components using Direct Iterative Reconstruction of Computed Tomography Trajectories," *Journal of Power Sources* **196**, 5293–5298 (2011).

- ¹⁴A. Kupsch, A. Lange, M. P. Hentschel, S. Lck, V. Schmidt, R. Grothausmann, A. Hilger, and I. Manke, "Missing wedge computed tomography by iterative algorithm DIRECTT," *Journal of Microscopy* **261**, 36–45 (2016).
- ¹⁵A. Rack, S. Zabler, B. R. Mller, H. Riesemeier, G. Weidemann, A. Lange, J. Goebbels, M. Hentschel, and W. Grner, "High resolution synchrotron-based radiography and tomography using hard X-rays at the BAMline (BESSY II)," *Nuclear Instruments and Methods in Physics Research Section A: Accelerators, Spectrometers, Detectors and Associated Equipment* **586**, 327–344 (2008).
- ¹⁶S. Evsevlev, T. Mishurova, S. Cabeza, R. Koos, I. Sevostianov, G. Garces, G. Requena, R. Fernandez, and G. Bruno, "The role of intermetallics in stress partitioning and damage evolution of AlSi₁₂CuMgNi alloy," *Materials Science & Engineering A* **736**, 453–464 (2018).
- ¹⁷S. Evsevlev, S. Cabeza, T. Mishurova, G. Garc I. Sevostianov, G. Requena, M. Boin, M. Hofmann, and G. Bruno, "Stress-induced damage evolution in cast AlSi₁₂CuMgNi alloy with one and two ceramic reinforcements. Part II: Effect of reinforcement orientation," *Journal of Materials Science* **55**, 1049–1068 (2020).
- ¹⁸A. M. Al-Falahat, A. Kupsch, M. P. Hentschel, A. Lange, N. Kardjilov, H. Marktter, and I. Manke, "Correction approach of detector backlighting in radiography," *Review of Scientific Instruments* **90**, 125108 (2019).
- ¹⁹W. van Aarle, W. J. Palenstijn, J. Cant, E. Janssens, F. Bleichrodt, A. Dabravolski, J. De Beenhouwer, K. Joost Batenburg, and J. Sijbers, "Fast and flexible X-ray tomography using the ASTRA toolbox," *Optics Express* **24**, 25129–25147 (2016).
- ²⁰J. Gregor and T. Benson, "Computational analysis and improvement of SIRT," *IEEE Transactions on Medical Imaging* **27**, 918–924 (2008).
- ²¹M. R. Hestenes and E. Stiefel, "Methods of conjugate gradients for solving linear systems," *Journal of Research of the National Bureau of Standards* **49**, 409–436 (1952).
- ²²A. Kupsch, A. Lange, M. P. Hentschel, and B. R. Mller, "Improved computed tomography by variable desmearing," *Materials Testing* **52**, 394–400 (2010).
- ²³R. Grothausmann, G. Zehl, I. Manke, S. Fiechter, P. Bogdanoff, I. Dorbandt, A. Kupsch, A. Lange, M. P. Hentschel, G. Schumacher, and J. Banhart, "Quantitative structural assessment of heterogeneous catalysts by electron tomography," *Journal of the American Chemical Society* **133**, 18161–18171 (2011).
- ²⁴S. Lck, A. Kupsch, A. Lange, M. P. Hentschel, and V. Schmidt, "Statistical analysis of tomographic reconstruction algorithms by morphological image characteristics," *Image Analysis Stereology* **29**, 61–77 (2010).
- ²⁵M. P. Hentschel, A. Lange, A. Kupsch, and B. R. Mller, "Reconstruction of incomplete model data sets in computed tomography by DIRECTT algorithm," *Materials Testing* **52**, 668–675 (2010).
- ²⁶C. E. Shannon, "A mathematical theory of communication," *Bell System Technical Journal* **27**, 379–423 (1948).
- ²⁷S. Allner, A. Gustschin, A. Fehrer, P. B. No and F. Pfeiffer, "Metric-guided regularisation parameter selection for statistical iterative reconstruction in computed tomography," *Scientific Reports* **9**, 6016 (2019).
- ²⁸J. L. Rodgers and W. A. Nicewander, "Thirteen ways to look at the correlation coefficient," *The American Statistician* **42**, 59–66 (1988).
- ²⁹Z. Wang and A. C. Bovik, "Mean squared error: Love it or leave it? A new look at signal fidelity measures," *IEEE Signal Processing Magazine* **26**, 98–117 (2009).
- ³⁰Z. Wang and A. C. Bovik, "A universal image quality index," *IEEE Signal Processing Letters* **9**, 81–84 (2002).
- ³¹Z. Wang, A. C. Bovik, H. R. Sheikh, and E. P. Simoncelli, "Image quality assessment: from error visibility to structural similarity," *IEEE Transactions on Image Processing* **13**, 600–612 (2004).

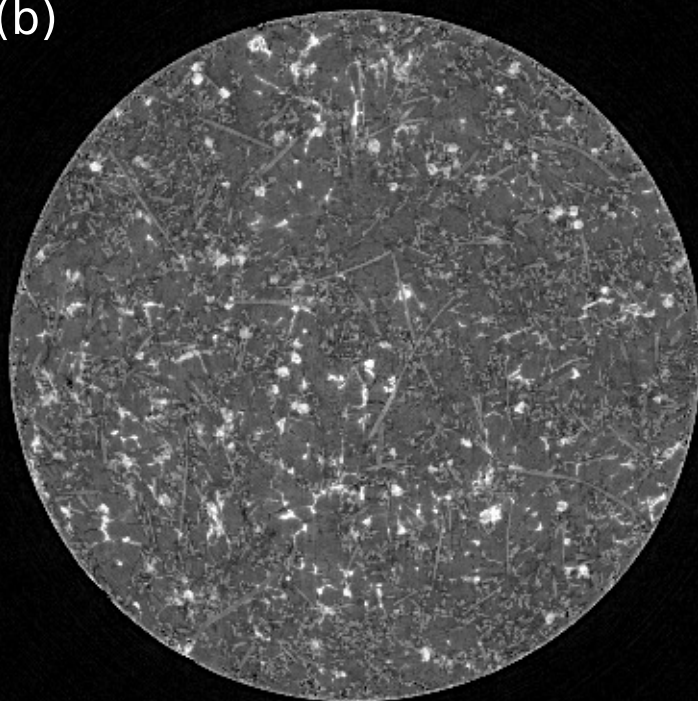




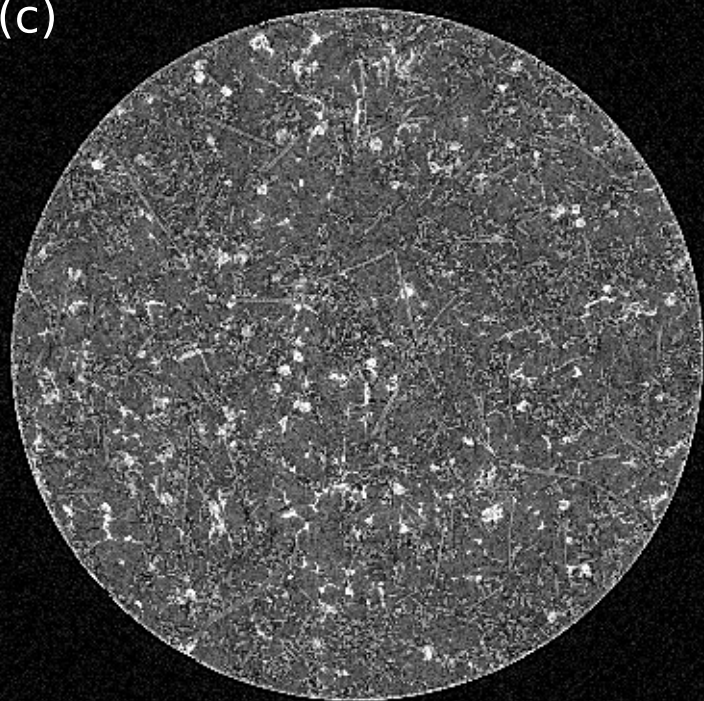
(a)



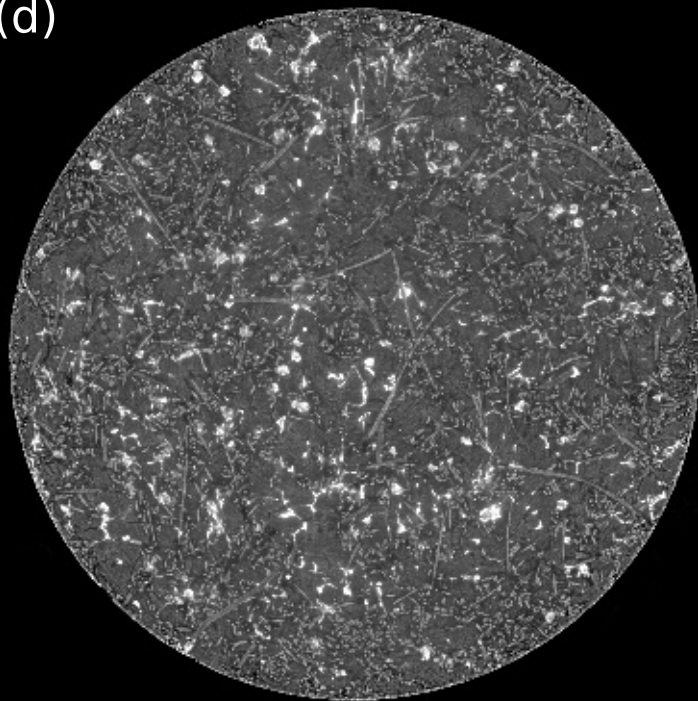
(b)



(c)



(d)



$\mu / 10^{-4}$

4

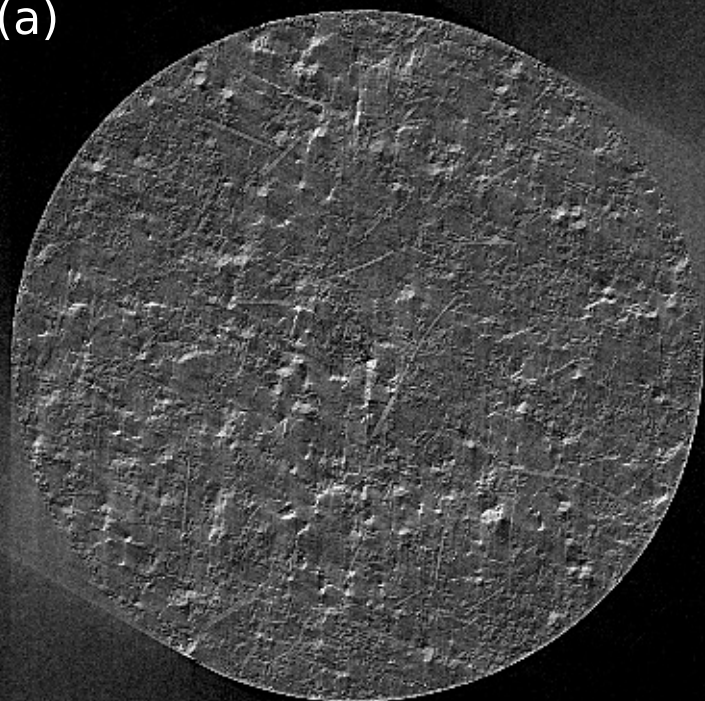
3

2

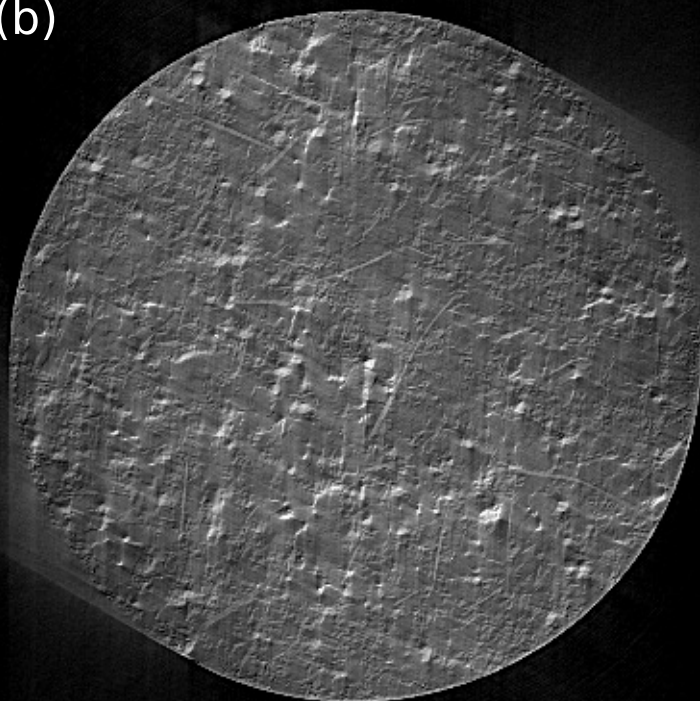
1

0

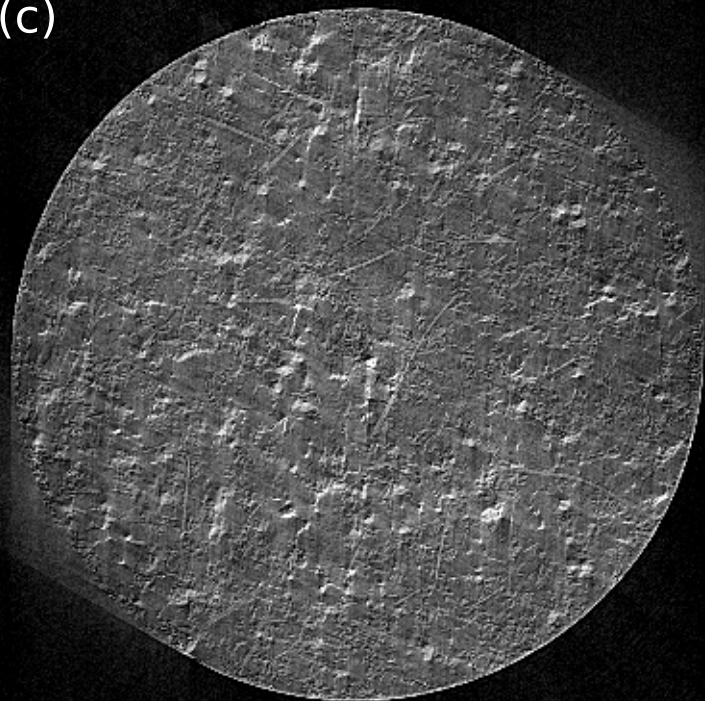
(a)



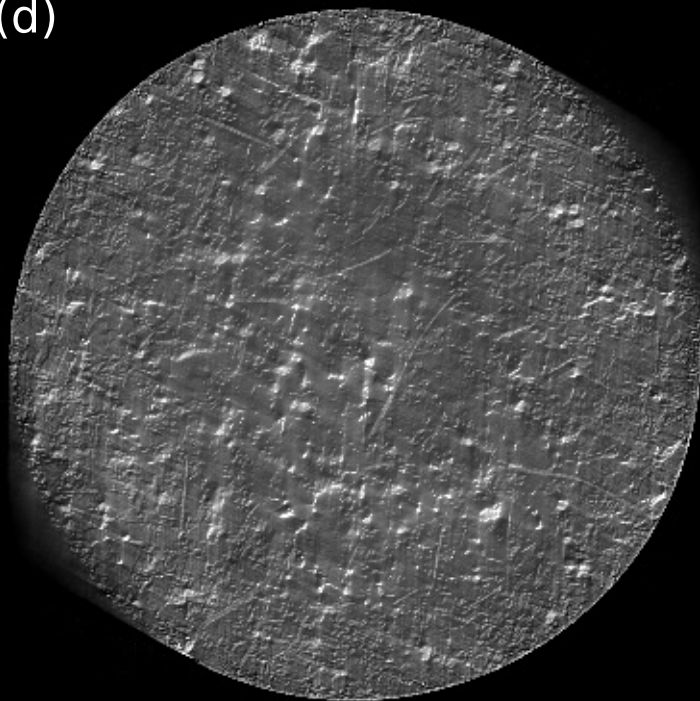
(b)



(c)



(d)



$\mu / 10^{-4}$

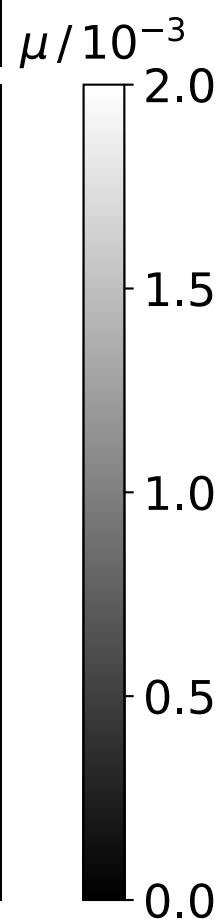
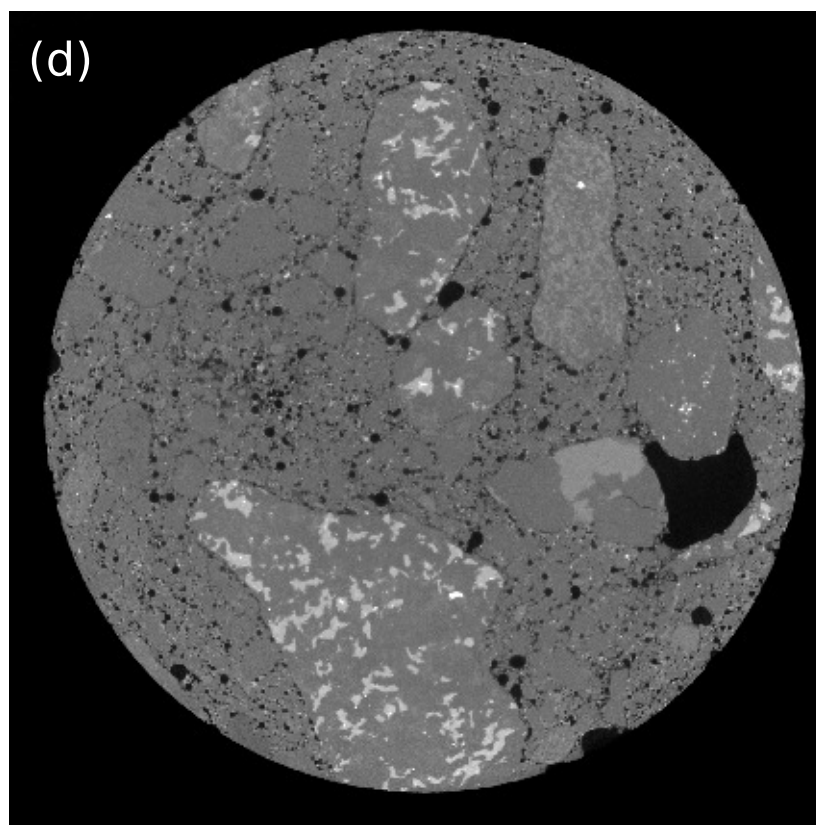
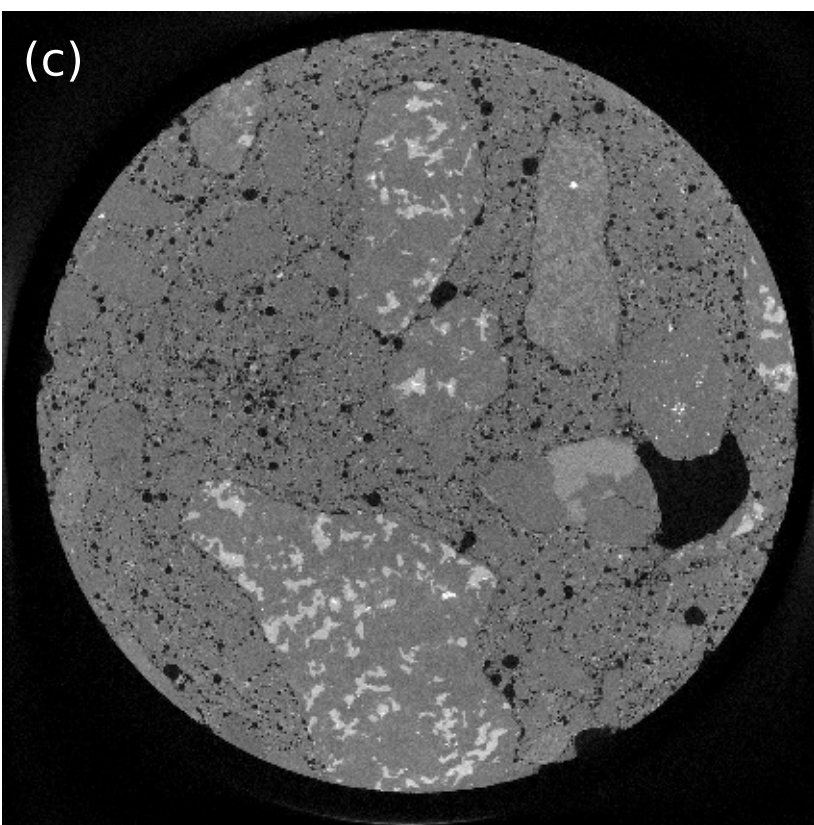
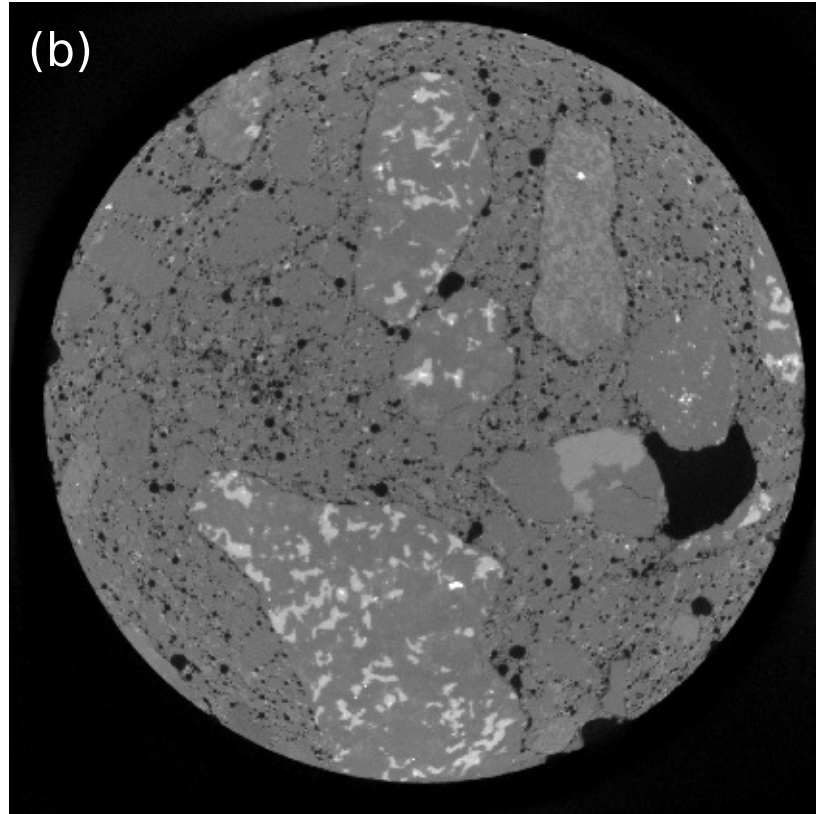
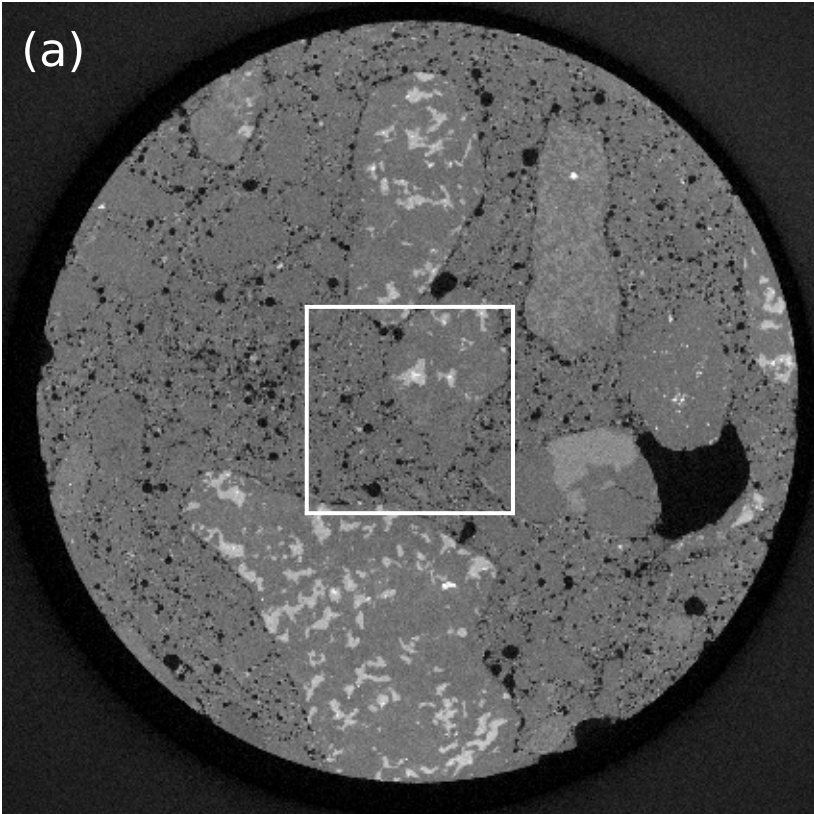
4

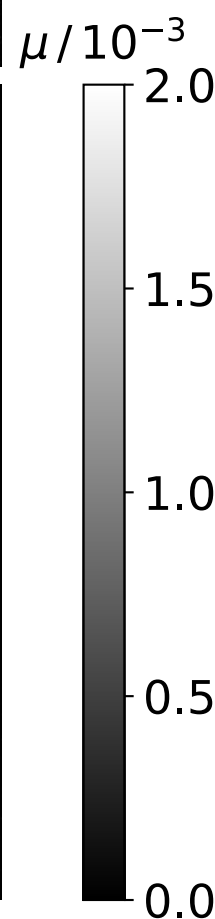
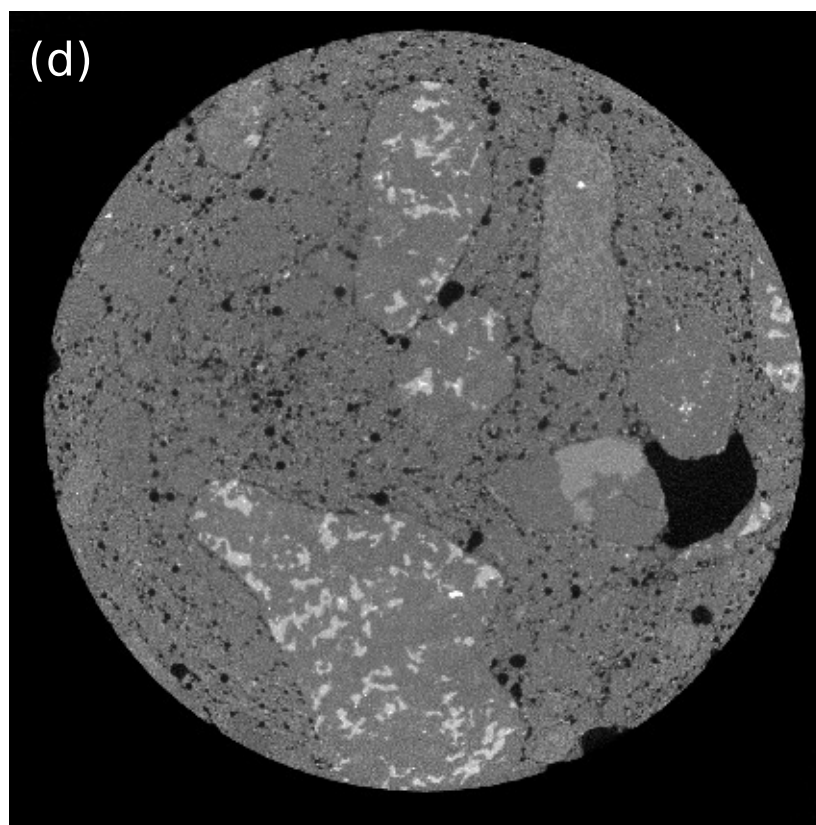
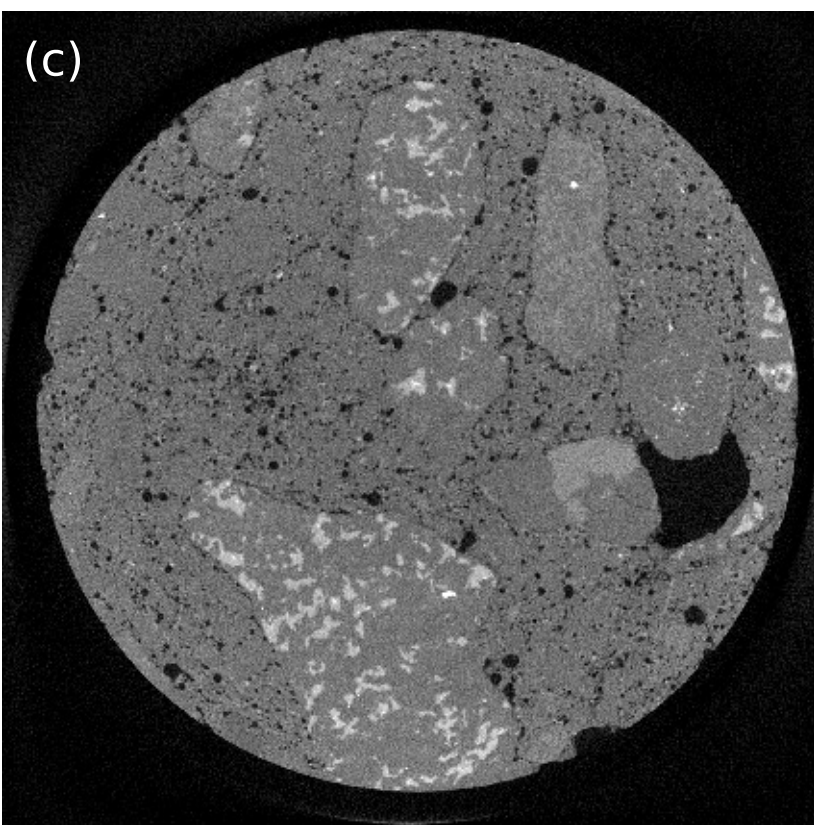
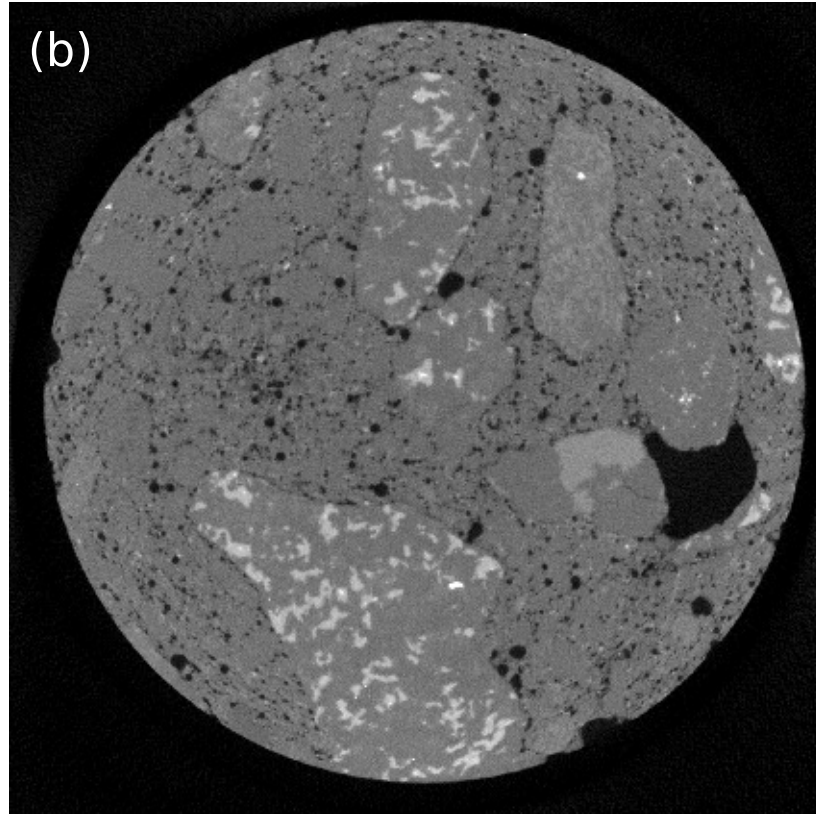
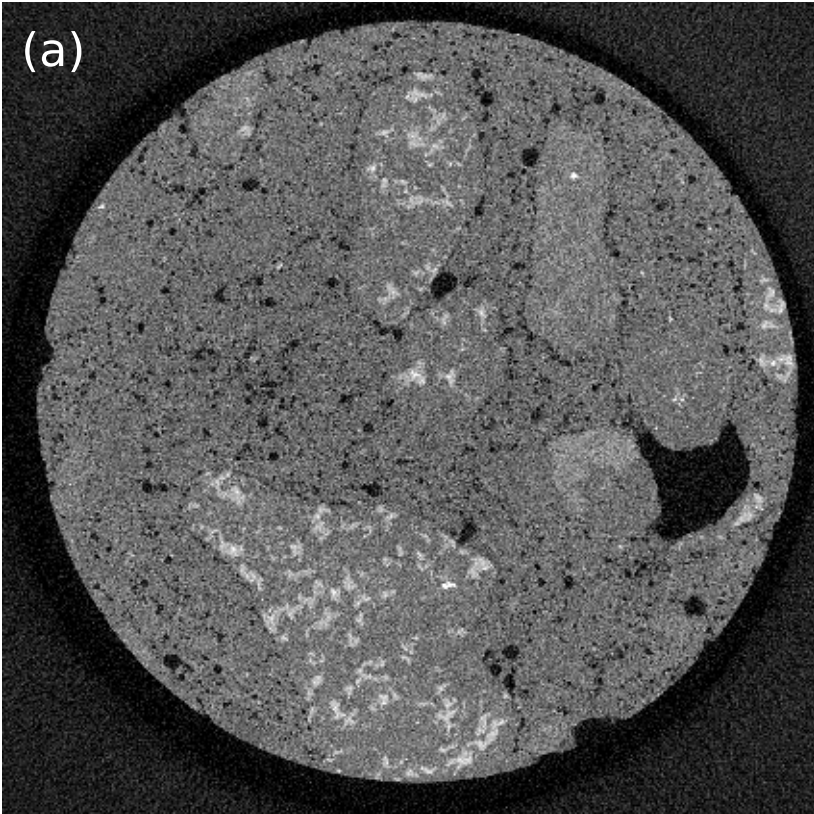
3

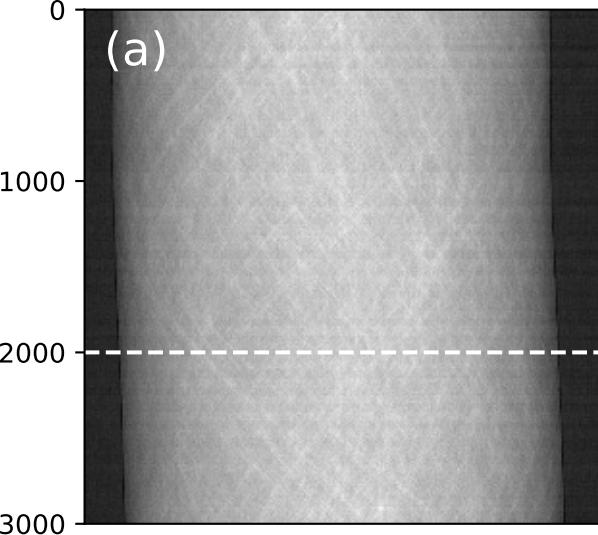
2

1

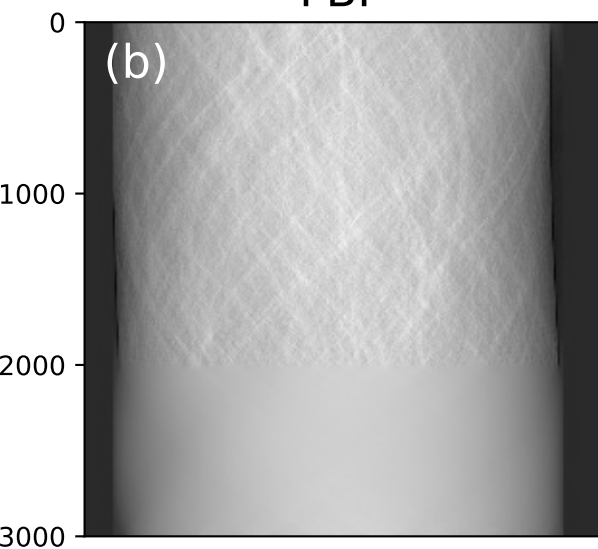
0



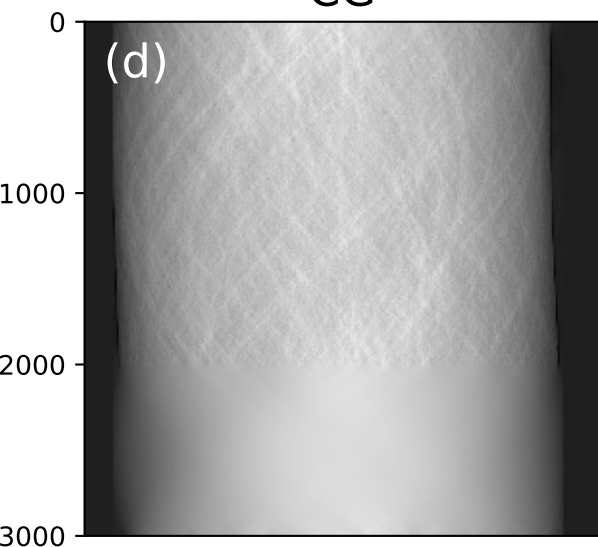




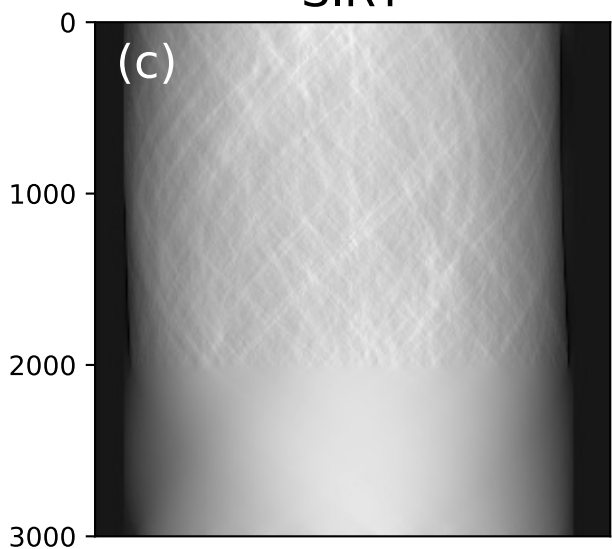
FBP



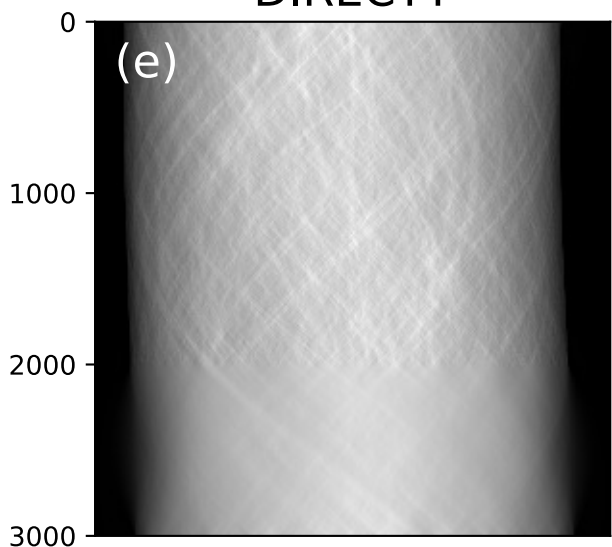
CG



SIRT

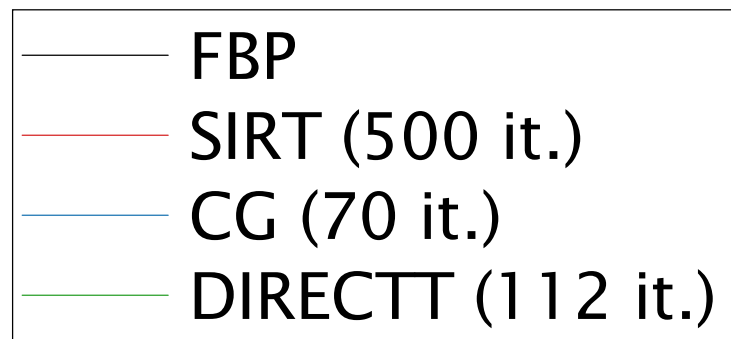


DIRECTT



PCC to measured projections

1.00
0.99
0.98



Projection angle (°)

